Map of low-frequency electromagnetic noise in the sky

M. Füllekrug, A. Mezentsev, R. Watson, Stéphane Gaffet, I. Astin, N. Smith, A. Evans

AGU PUBLICATIONS

Geophysical Research Letters

RESEARCH LETTER
10.1002/2015GL064142

Key Points:
- A reference map for anthropogenic noise in the sky is established
- Noise sources are located at elevation angles well above the horizon
- Exclusion zones are observed at local zenith and southwest of the array

Supporting Information:
- Tables S1 and S2

Correspondence to:
M. Füllekrug,
eesmf@bath.ac.uk

Citation:
Füllekrug, M., A. Mezentsev, R. Watson, S. Gaffet, I. Astin, N. Smith, and A. Evans (2015), Map of low-frequency electromagnetic noise in the sky, *Geophys. Res. Lett.*, *42*, 4648–4653, doi:10.1002/2015GL064142.

Received 9 APR 2015
Accepted 11 MAY 2015
Accepted article online 19 MAY 2015
Published online 4 JUN 2015

Map of low-frequency electromagnetic noise in the sky

Martin Füllekrug[1], Andrew Mezentsev[1], Robert Watson[1], Stéphane Gaffet[2], Ivan Astin[1], Nathan Smith[1], and Adrian Evans[1]

[1]Department of Electronic and Electrical Engineering, Centre for Space, Atmospheric and Oceanic Science, University of Bath, Bath, UK, [2]Laboratoire Souterrain à Bas Bruit (LSBB), UMS, Université of Avignon, CNRS, La Grande Combe, Rustrel, France

Abstract The Earth's natural electromagnetic environment is disturbed by anthropogenic electromagnetic noise. Here we report the first results from an electromagnetic noise survey of the sky. The locations of electromagnetic noise sources are mapped on the hemisphere above a distributed array of wideband receivers that operate in a small aperture configuration. It is found that the noise sources can be localized at elevation angles up to ∼60° in the sky, well above the horizon. The sky also exhibits zones with little or no noise that are found toward the local zenith and the southwest of the array. These results are obtained by a rigorous analysis of the residuals from the classic dispersion relation for electromagnetic waves using an array analysis of electric field measurements in the frequency range from ∼20 to 250 kHz. The observed locations of the noise sources enable detailed observations of ionospheric modification, for example, caused by particle precipitation and lightning discharges, while the observed exclusion zones enable the detection of weak natural electromagnetic emissions, for example, from streamers in transient luminous events above thunderclouds.

1. Introduction

The Earth's natural electromagnetic environment from ∼1 Hz to ∼300 MHz is dominated by broadband pulse sequences emanating from lightning discharges [e.g., *Füllekrug and Fraser-Smith*, 2011; *Fraser-Smith and Bowen*, 1992; *Lanzerotti et al.*, 1990, 1989]. The observation of weaker natural electromagnetic signals is increasingly confined to remote areas [*Fraser-Smith et al.*, 1992] because these signals are superimposed on disturbing electromagnetic noise sources from man made communication transmitters operating in relatively narrow frequency bands ranging from ∼100 Hz around ∼20 kHz to ∼10 kHz near ∼250 kHz, i.e., with a typical bandwidth of ∼10 % of the carrier frequency. The locations of these electromagnetic noise sources are closely monitored and mapped around the world by the use of sensitive electromagnetic recordings on board of satellites. For example, the electromagnetic radiation from transmitters for submarine communication [*Sauvaud et al.*, 2008] and marine navigation [*Füllekrug et al.*, 2011, 2009] escapes from the Earth ionosphere waveguide into near-Earth space in the Whistler mode [e.g., *Lefeuvre et al.*, 2013; *Helliwell*, 1965]. These low-frequency radio communication transmitters are widely used for geophysical exploration, for example, to study particle precipitation from the radiation belts into the Earth's atmosphere and the impact of lightning discharges on the upper atmosphere [e.g., *Denton et al.*, 2014; *Haldoupis et al.*, 2013, 2012; *Sauvaud et al.*, 2008; *Inan et al.*, 2007; *Horne et al.*, 2005, and references therein].

However, global maps of electromagnetic noise sources do not provide any information on how electromagnetic noise sources would be perceived at a given location which is relevant for living beings on planet Earth. Answering this important question is a responsibility which falls squarely into the area of geophysical research in order to constraint speculation. For example, it was recently reported that European robins, *Erithacus rubecula*, have a receptor for anthropogenic electromagnetic noise that inhibits natural migratory behavior [*Engels et al.*, 2014], i.e., well below the action limit for maximum permissible exposure [e.g., *IEEE International Committee on Electromagnetic Safety (SCC39)*, 2010, 2005, Figure 4]. This conclusion was demonstrated by the efficiency of a Faraday cage to restore natural migratory behavior. These observations thereby lend to the question what the spatial distribution of anthropogenic electromagnetic noise at a given location actually is.

Another geophysical application for mapping electromagnetic noise sources in the sky is to identify areas with little or no electromagnetic noise to facilitate the detection and location of the weak natural electromagnetic emissions emanating from the growth and branching of streamers in sprite discharges above thunderclouds [*Füllekrug et al.*, 2013] that have been predicted based on a theoretical analysis of transient luminous events [*Qin et al.*, 2012; *Pasko*, 2010]. Yet it was only recently suggested to investigate the context of these challenging observations with a novel analysis that uses a small aperture array [*Füllekrug et al.*, 2014]. The small aperture array determines the wave number vector (length and direction) of distant electromagnetic radiation sources, while a lightning detection network aims to determine lightning source locations inside, or in the proximity of, the network [e.g., *Lyu et al.*, 2014; *Wu et al.*, 2014; *Stock et al.*, 2014; *Rakov*, 2013; *Bitzer et al.*, 2013; *Mezentsev and Füllekrug*, 2013, and references therein]. This contribution extends our initial work on small aperture arrays to establish a reference map for anthropogenic electromagnetic noise sources in the sky that can assist the detection and location of relatively weak natural electromagnetic signals above thunderclouds.

2. Theory

The local electromagnetic field $E(t)$ of a distant electromagnetic noise source sweeps as a plane wave $\exp^{-i(\boldsymbol{k}\boldsymbol{r_n}-\omega t)}$ across an array of $n = 1, 2, \dots, N$ wideband receivers such that the measurements

$$y(\boldsymbol{r_n}, t) = E(t)e^{-i(\boldsymbol{k}\boldsymbol{r_n}-\omega t)}, \tag{1}$$

depend on the n'th receiver location $\boldsymbol{r_n}$ and time t. In this description, the wave number vector $\boldsymbol{k}$ is related to the frequency ω through the dispersion relation $k = s\omega$, where s is the slowness of the electromagnetic wave during the propagation across the array. The plane wave description corresponds effectively to a transfer function between the electromagnetic source field E and the measurements y. This ansatz results in unique solutions for the wave number vector and the electromagnetic source field if the wave number $k < k_F$, where $k_F = 2\pi/(2d_{\max})$ is the fundamental wave number inferred from the maximum distance $d_{\max}$ between two receivers in the array. For larger wave numbers, phase ambiguities can occur such that no unique solution can be determined without a modification of the ansatz in equation (1). Larger wave numbers correspond to larger frequencies with $k = \omega/c$, where c is the speed of light, such that the certainty relation $k < k_F$ can be reformulated for the frequency of the electromagnetic wave $f < c/(2d_{\max})$. For example, an array with a maximum distance of 1200 m between two receivers allows for an array analysis with a maximum frequency of 125 kHz without phase ambiguities. Similarly, for a target frequency of 250 kHz, the maximum distance between two receivers in the array should not exceed 600 m.

This contribution aims to determine a sky map of electromagnetic noise sources from ~20 to 250 kHz with the small aperture array at Charmy Down near Bath in southwest England that has a maximum distance ~1261.4 m between two receivers [*Füllekrug et al.*, 2014; *Mezentsev and Füllekrug*, 2013]. It is therefore necessary to multiply equation (1) with a reference plane wave $e^{i(\boldsymbol{k_0}\boldsymbol{r_n}-\omega t)}$ to avoid phase ambiguities

$$y_c(\boldsymbol{r_n}, t) = Ee^{-i(\boldsymbol{k}-\boldsymbol{k_0})\boldsymbol{r_n}}. \tag{2}$$

The multiplication of the measurements with the reference plane wave results in a complex time series $y_c = ye^{i(\boldsymbol{k_0}\boldsymbol{r_n}-\omega t)}$ with a phase that is always referenced to the start time of the recordings after application of a low-pass filter. The spatial phase progression $e^{i\boldsymbol{k_0}\boldsymbol{r_n}}$ across the network ensures that the phase of the complex time series is also referenced to the maximum of the array aperture

$$T(\Delta\boldsymbol{k}, \boldsymbol{r_n}) = \frac{1}{N}\sum_{n=1}^{N} e^{-i\Delta\boldsymbol{k}\boldsymbol{r_n}}, \tag{3}$$

where $\Delta\boldsymbol{k} = \boldsymbol{k} - \boldsymbol{k_0}$. This array aperture T is the response of the array to an electromagnetic wave arriving from the local zenith, where each summand is a basis function of the corresponding sparse spatial Fourier transform. The array aperture describes how well the array focuses a collimated electromagnetic wave onto the wave number domain and whether any ambiguities can occur during the interpretation. The multiplication of the original array aperture with the spatial phase progression effectively translates the maximum of the array aperture toward the position of the reference plane wave and thereby avoids any phase ambiguities (Figure 1, left). For example, it is possible to use the reference wave number vector $\boldsymbol{k_0} = k_0(\cos\Phi, \sin\Phi)^T$, where Φ is the arrival angle calculated from a wave propagation along the great circle path from the source to the receiver, if the location of the source is known. If the location of the source is not known, it is possible

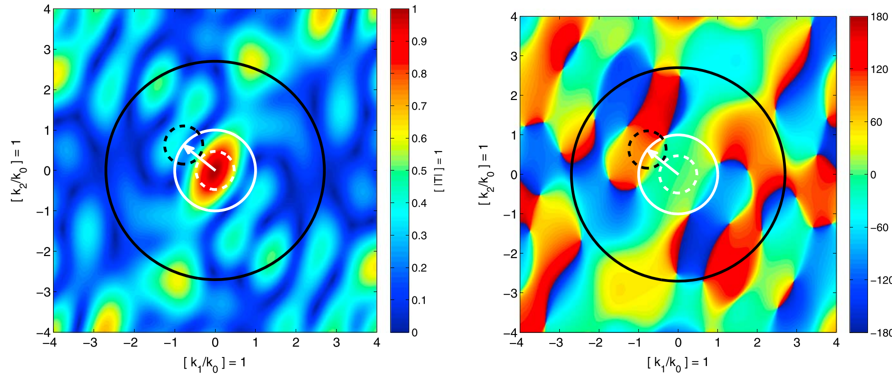

Figure 1. The array aperture. (left) The region of interest for the analysis (white solid circle) lies outside the fundamental wave number k_F (white dashed circle). The translation of the array aperture by the reference wave number vector $\boldsymbol{k_0}$ (arrow) ensures that the certainty relation $k < k_F$ (black dashed circle) applies to the region of interest such that no phase ambiguities occur. The Nyquist wave number k_N (black solid circle) defines the maximum possible area for the array analysis. (right) The phase of the aperture varies smoothly for wave numbers within the region where the certainty relation $k < k_F$ applies (white dashed circle).

to apply the Progressive Multiple Channel Correlation (PMCC) method [*Cansi*, 1995] or to vary Φ and k_0 until a solution without phase ambiguities is found. The translation of the array aperture has the added benefit that the phase of the aperture varies smoothly for wave numbers within the region where the certainty relation $k < k_F$ applies (Figure 1, right). Finally, equation (2) is formulated for the phase such that

$$(x_{1,n}, x_{2,n}, 1)\begin{pmatrix}\Delta k_1\\ \Delta k_2\\ \phi\end{pmatrix} = \varphi_n + \delta\varphi_n \quad \wedge \quad n = 1, 2, \ldots N = 10, \tag{4}$$

where $x_{1,n}$ and $x_{2,n}$ are the n'th receiver location coordinates in the east and north directions, ϕ is the phase of the electromagnetic source field, and φ_n is the observed phase of the referenced complex time series. Equation (4) is solved with the Gaussian method of least squares to minimize the phase residuals $\delta\varphi_n$ such that the resulting wave number vectors are finally calculated from $\boldsymbol{k} = \Delta\boldsymbol{k} + \boldsymbol{k_0}$.

3. Mapping Electromagnetic Noise Sources

To map electromagnetic noise sources in the sky, we make use of recordings with an array of 10 wideband receivers that are distributed over an area of ~1×1 km on Charmy Down airfield near Bath in the UK [*Füllekrug et al.*, 2014; *Mezentsev and Füllekrug*, 2013]. Here we make use of 48 electromagnetic noise sources for the analysis which is divided into two parts (Tables S1 and S2 in the supporting information). The first part uses the center frequencies and geographic coordinates of 26 (54%) noise sources. The second part uses only the center frequencies of the other 22 (46%) noise sources. The mapping of these noise sources requires a determination of their locations onto the hemisphere above the array by use of the inferred wave number vectors which vary with time. As a result, the wave number vectors for each sample are integrated over time such that a bivariate distribution function in the wave number plane $k_1 \times k_2$ develops for each individual electromagnetic noise source. These bivariate distributions tend to exhibit an elliptical scatter pattern (Figure 2, left). The bivariate character of the distribution function enables a determination of the two standard deviations in the directions of the major and minor axes of the distribution by use of the covariance matrix. The covariance matrix $\boldsymbol{C}$ is composed of the expectation values for the autocovariance and cross covariance, and it can be decomposed into the variances along the major and minor axes by an eigenvalue analysis

$$\boldsymbol{C} = \begin{pmatrix} < k_1, k_1 > & < k_1, k_2 > \\ < k_2, k_1 > & < k_2, k_2 > \end{pmatrix} = \boldsymbol{R}\lambda\boldsymbol{R}^T. \tag{5}$$

The major and minor axes of the scatter ellipse are given by the first and second column of the rotation matrix $\boldsymbol{R}$ such that the orientation of the major axis with respect to the east direction is given by $\phi_e = \arctan(r_{2,1}/r_{1,1})$. The standard deviations along the major and minor axes (max and min) are calculated from the diagonal

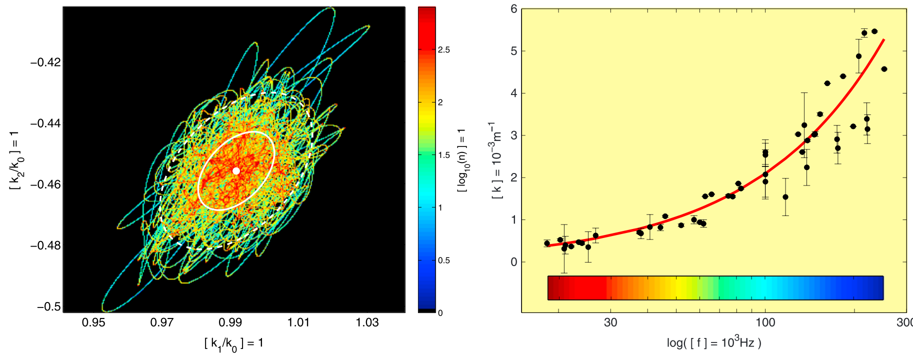

Figure 2. Certainty of wave numbers. (left) Example of a bivariate distribution function of the observed wave numbers from a typical electromagnetic noise source. The center (white dot) is the most likely, or median, wave number. The standard deviations along the major and minor axes of the scatter ellipse (solid line) include ∼68.2% of the observed wave numbers. The 2σ contour (dashed line) includes ∼95.4% of all wave numbers. (right) The dispersion relation for 48 electromagnetic noise sources (dots) exhibits significant deviations from the classic dispersion relation with a slowness corresponding to the speed of light (line). Each electromagnetic noise source is assigned to a color code depending on its frequency (color bar).

elements of the eigenvalue matrix λ by using $\sigma_{max} = \sqrt{\lambda_{max}}$ and $\sigma_{min} = \sqrt{\lambda_{min}}$. The position of the wave number vector is then given by the most likely, or median, position with an uncertainty determined by the geometric mean of the standard deviations along the major and minor axis $\sigma = \sqrt{\sigma_{max}\sigma_{min}}$. The median positions of 48 electromagnetic noise sources and their uncertainties can be compared to the classic dispersion relation $k_c = s\omega$ with the slowness $s = 1/c$ corresponding to the speed of light (Figure 2, right). It is evident that significant deviations from the classic dispersion relation occur. These residuals are attributed to the physical properties of each individual electromagnetic noise source, i.e., the superposition of the transverse electric and transverse magnetic electromagnetic wave propagation modes (TE_n/TM_n), and possibly an influence of the Earth's geomagnetic field [*Barr et al.*, 2000]. Each electromagnetic noise source is assigned to a color code on a logarithmic frequency scale to reflect the energy of the radiation, i.e., reddish colors are allocated to small frequencies with low energies, whereas bluish colors are allocated to large frequencies with high energies.

The median positions of the 48 electromagnetic noise sources exhibit a distinct distribution in the plane of normalized wave numbers (Figure 3, left). Most of the noise sources are located within the unit circle, which is indicative of electromagnetic waves arriving from an elevation angle at the array. Some electromagnetic noise sources are located outside of the unit circle which indicates that the electromagnetic waves from these sources have propagation speeds smaller than the speed of light. All of these electromagnetic noise sources lie within a circle with a radius $k/k_0 < 1.25$ which places a lower limit on the electromagnetic wave propagation speed for waves from ∼20 to 250 kHz. This lower limit defines a horizon for mapping electromagnetic noise sources in the sky. The elevation angle of a noise source above the horizon is given by $\Theta = \arccos(k/k_m)$, where k_m is the limiting wave number, i.e., the largest wave number with the smallest electromagnetic wave propagation speed in the medium near the array. This step finally enables a mapping of the locations of electromagnetic noise sources on the hemisphere above the array. Each pixel of the wave number plane is mapped to the corresponding spherical coordinates $\hat{\mathbf{e}}_\mathbf{r} = (\cos\Theta\cos\Phi, \cos\Theta\sin\Phi, \sin\Theta)^T$, where Φ is the arrival angle of the electromagnetic wave measured with respect to the geographic east and Θ is the elevation angle measured from the horizon toward the electromagnetic noise source.

The resulting map of electromagnetic noise sources in the sky exhibits a distinct distribution with well-defined areas of electromagnetic noise and areas without electromagnetic noise (Figure 3, right). The total area covered by the electromagnetic noise sources is only a small fraction of the total. Many electromagnetic noise sources are found toward the northwest, north, east, and southeast directions. The area toward the southwest with almost no electromagnetic noise sources corresponds to the Atlantic Ocean with little anthropogenic activity. Another area without electromagnetic noise sources is found toward the local zenith above the array because the electromagnetic noise sources are located at elevation angles that range from 0° up to ∼60°. The observed exclusion zones thereby offer novel windows of opportunities toward the search for yet unknown electromagnetic sources in the sky.

10.1002/2015GL064142

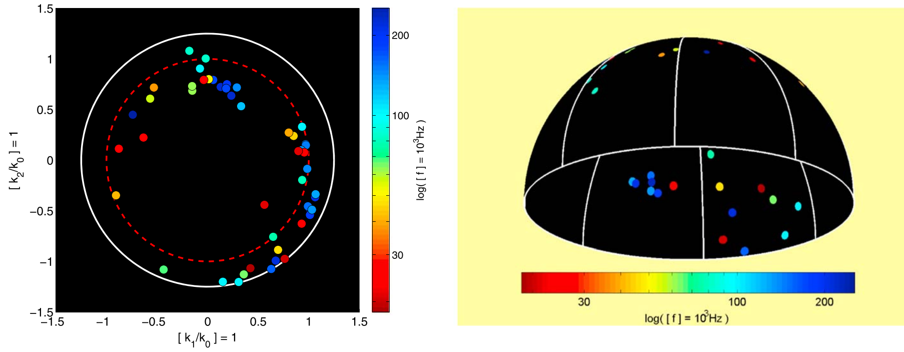

Figure 3. Mapping of electromagnetic noise sources. (left) The median positions of 48 electromagnetic noise sources exhibit a distinct distribution in the plane of normalized wave numbers. Many noise sources lie within the unit circle (dashed line) which corresponds to the classic dispersion relation. All noise sources lie within the circle $k/k_0 = 1.25$ (solid line) that defines a horizon for the noise sources. The positions of the noise sources are independent of their frequency indicated by the color code. (right) The electromagnetic noise sources are mapped on a hemisphere above the array. The map exhibits a distinct distribution with well-defined areas of electromagnetic noise and areas without electromagnetic noise. Many noise sources occur at large elevation angles up to $\sim 60°$.

4. Discussion

The locations of electromagnetic noise sources are determined here from the most likely, or median, positions of bivariate distribution functions in the wave number plane. As a result, the uncertainties of the positions are not taken into account for the mapping of noise sources in the sky. The rationale behind this approach is that the physical origin of the observed uncertainties is not yet well understood. For example, the uncertainties might result from a superposition of different apparent locations of electromagnetic noise sources in the sky. Another possibility is that the observed uncertainties reflect random fluctuations around the true source location. It is possible to assess the uncertainty of the source location in a first order approximation for electromagnetic waves which arrive almost from the horizon and travel during the time t across the baseline $b = d_{max}$ of the array such that the phase of the wave is determined by $kb = \omega t$. In this case, the experimental timing accuracy results in an uncertainty of the wave number

$$\frac{d}{dt}k = \frac{\omega}{b} \quad \rightarrow \quad \delta k = k_0 \frac{c}{b} \delta t. \tag{6}$$

For example, the Charmy Down network has a baseline of $b \approx 1.2$ km and a clock jitter $\delta t \approx 20$ns [*Füllekrug et al.*, 2014] such that $\delta k/k_0 \approx 5 \cdot 10^{-3}$. This result strongly suggests that the observed wave number uncertainties are most likely of natural origin (Figure 2, left). From a theoretical point of view, the uncertainty of the wave number is determined by the geometry of the experiment $k = k_0 \cos(h/d)$, where h is the height of the electromagnetic noise source above the ground and d is the horizontal distance between the array and the footprint of the noise source on the ground. For small elevation angles $\Theta \approx h/d$, the cosine can be expanded to $\cos(h/d) = 1 - \frac{1}{2}(h/d)^2$ such that

$$\frac{d}{dh}k = -k_0 \frac{h}{d^2} \quad \rightarrow \quad \delta k = -k_0 \frac{h}{d^2} \delta h. \tag{7}$$

Substituting equation (6) into equation (7) and solving for the height uncertainty δh finally result in

$$\delta h = -\frac{c}{b}\frac{d^2}{h}\delta t. \tag{8}$$

For example, the height uncertainty is ~ 10 km for the baseline of the Charmy Down network ~ 1.2 km and a sprite at ~ 60 km height which is ~ 400 km away. Similarly, the height uncertainty is ~ 1 km for a baseline of ~ 12 km during typical field work for sprite research [*Mezentsev and Füllekrug*, 2013]. This analysis of the height uncertainty for typical network geometries shows that small aperture arrays have the capability to be used for the benefit of sprite research.

5. Summary

Fourty-eight electromagnetic noise sources of anthropogenic origin were successfully mapped in the sky above an array of wideband receivers operating in a small aperture configuration. The spatial distribution of the electromagnetic noise sources shows the absence of anthropogenic noise sources toward the southwest and local zenith, i.e., the Atlantic Ocean and space. These exclusion zones offer novel windows of opportunities toward the search for natural electromagnetic signal sources in the sky such as the weak electromagnetic emissions from streamers in transient luminous events above thunderclouds.

Acknowledgments

The work of M.F., A.M., and R.W. is sponsored by the Natural Environment Research Council (NERC) under grants NE/L012669/1 and NE/H024921/1. S.G. is supported by CNRS. The data used for this publication are available upon request from eesmf@bath.ac.uk. M.F. wishes to thank David Ll. Jones, Elisabeth Blanc, and Gerhard Müller for inspiration and encouragement to pursue this project and acknowledges helpful discussions with Frank Tschepke, Antony Fraser-Smith, Michael Stock, and Daniel Kotovsky.

The Editor thanks Robert Moore and an anonymous reviewer for their assistance in evaluating this paper.

References

Barr, R., D. Jones, and C. Rodger (2000), ELF and VLF radio waves, *J. Atmos. Sol. Terr. Phys.*, *62*(17–18), 1689–1718, doi:10.1016/S1364-6826(00)00121-8.

Bitzer, P., H. Christian, M. Stewart, J. Burchfield, S. Podgorny, D. Corredor, J. Hall, E. Kuznetsov, and V. Franklin (2013), Characterization and applications of VLF/LF source locations from lightning using the Huntsville Alabama Marx Meter Array, *J. Geophys. Res.*, *118*, 3120–3138, doi:10.1002/jgrd.50271.

Cansi, Y. (1995), An automatic seismic event processing for detection and location: The P.M.C.C method, *Geophys. Res. Lett.*, *22*(9), 1021–1024, doi:10.1029/95GL00468.

Denton, M., M. Kosch, J. Borovsky, M. Clilverd, R. Friedel, and T. Ulich (2014), First optical observations of energetic electron precipitation at 4278 Å caused by a powerful VLF transmitter, *Geophys. Res. Lett.*, *41*, 1–6, doi:10.1002/2014GL059553.

Engels, S., N.-L. Schneider, N. Lefeldt, C. M. Hein, M. Zapka, A. Michalik, D. Elbers, A. Kittel, P. J. Hore, and H. Mouritsen (2014), Anthropogenic electromagnetic noise disrupts magnetic compass orientation in a migratory bird, *Nature*, *509*, 353–356, doi:10.1038/nature13290.

Fraser-Smith, A., and M. Bowen (1992), The natural background levels of 50/60 Hz radio noise, *IEEE Trans. Electromagn. Compat.*, *34*(3), 330–337.

Fraser-Smith, A., R. Helliwell, L. Lanzerotti, and T. Rosenberg (1992), Antarctic environmental concerns, *Science*, *256*, 949–950.

Füllekrug, M., and A. Fraser-Smith (2011), The Earth's electromagnetic environment, *Geophys. Res. Lett.*, *38*, L21807, doi:10.1029/2011GL049572.

Füllekrug, M., M. Parrot, M. Ash, I. Astin, P. Williams, and R. Talhi (2009), Transionospheric attenuation of 100 kHz radio waves inferred from satellite and ground based observations, *Geophys. Res. Lett.*, *36*, L06104, doi:10.1029/2008GL036988.

Füllekrug, M., C. Hanuise, and M. Parrot (2011), Experimental simulation of satellite observations of 100 kHz radio waves from relativistic electron beams above thunderclouds, *Atmos. Chem. Phys.*, *11*, 1–7, doi:10.5194/acp-11-1-2011.

Füllekrug, M., A. Mezentsev, S. Soula, O. van der Velde, and T. Farges (2013), Sprites in low frequency radio noise, *Geophys. Res. Lett.*, *40*, 1–5, doi:10.1002/grl.50408.

Füllekrug, M., A. Mezentsev, R. Watson, S. Gaffet, I. Astin, and A. Evans (2014), Array analysis of electromagnetic radiation from radio transmitters for submarine communication, *Geophys. Res. Lett.*, *41*, 1–7, doi:10.1002/2014GL062126.

Haldoupis, C., M. Cohen, B. Cotts, E. Arnone, and U. Inan (2012), Long-lasting D-region ionospheric modifications, caused by intense lightning in association with elve and sprite pairs, *Geophys. Res. Lett.*, *39*, L16801, doi:10.1029/2012GL052765.

Haldoupis, C., M. Cohen, E. Arnone, B. Cotts, and S. Dietrich (2013), The VLF fingerprint of elves: Step-like and long-recovery early VLF perturbations caused by powerful ±CG lightning EM pulses, *J. Geophys. Res.*, *118*, 1–11, doi:10.1002/jgra.50489.

Helliwell, R. (1965), *Whistlers and Related Ionospheric Phenomena*, Stanford Univ. Press, Calif.

Horne, R., et al. (2005), Wave acceleration of electrons in the Van Allen radiation belts, *Nature*, *437*, 1–4, doi:10.1038/nature03939.

IEEE International Committee on Electromagnetic Safety (SCC39) (2005), IEEE standard for safety levels with respect to human exposure to radio frequency electromagnetic fields, 3 kHz to 300 GHz, *Inst. Electr. Electron. Eng.*, 1–250.

IEEE International Committee on Electromagnetic Safety (SCC39) (2010), IEEE standard for safety levels with respect to human exposure to radio frequency electromagnetic fields, 3 kHz to 300 GHz. Amendment 1: Specifies ceiling limits for induced and contact current, clarifies distinctions between localized exposure and spatial peak power density, *Inst. Electr. Electron. Eng.*, 1–19.

Inan, U., D. Piddyachiy, W. Peter, J. Sauvaud, and M. Parrot (2007), DEMETER satellite observations of lightning-induced electron precipitation, *Geophys. Res. Lett.*, *34*, L07103, doi:10.1029/2006GL029238.

Lanzerotti, L., D. Thomson, C. MacLennan, K. Rinnert, E. Krider, and M. Uman (1989), Power spectra at radio frequency of lightning return stroke waveforms, *J. Geophys. Res.*, *94*(11), 13,221–13,227.

Lanzerotti, L., C. Maclennan, and A. Fraser-Smith (1990), Background magnetic spectra: $\sim 10^{-5}$ to $\sim 10^{5}$ Hz, *Geophys. Res. Lett.*, *17*(10), 1593–1596.

Lefeuvre, F., J. Pincon, and M. Parrot (2013), Midlatitude propagation of VLF to MF waves through nighttime ionosphere above powerful VLF transmitters, *J. Geophys. Res.*, *118*, 1210–1219, doi:10.1002/jgra.50177.

Lyu, F., S. A. Cummer, R. Solanki, J. Weinert, L. McTague, A. Katko, J. Barrett, L. Zigoneanu, Y. Xie, and W. Wang (2014), A low-frequency near-field interferometric-TOA 3-D Lightning Mapping Array, *Geophys. Res. Lett.*, *41*, 1–8, doi:10.1002/2014GL061963.

Mezentsev, A., and M. Füllekrug (2013), Mapping the radio sky with an interferometric network of low-frequency radio receivers, *J. Geophys. Res.*, *118*, 1–9, doi:10.1002/jgrd.50671.

Pasko, V. (2010), Recent advances in theory of transient luminous events, *J. Geophys. Res.*, *115*, A00E09, doi:10.1029/2009JA014860.

Qin, J., S. Celestin, and V. Pasko (2012), Low frequency electromagnetic radiation from sprite streamers, *Geophys. Res. Lett.*, *39*, L22803, doi:10.1029/2012GL053991.

Rakov, V. (2013), Electromagnetic methods of lighting detection, *Surv. Geophys.*, *34*, 731–735, doi:10.1007/s10712-013-9251-1.

Sauvaud, J., R. Maggiolo, C. Jacquey, M. Parrot, J. Berthelier, R. Gamble, and C. Rodger (2008), Radiation belt electron precipitation due to VLF transmitters: Satellite observations, *Geophys. Res. Lett.*, *35*, L09101, doi:10.1029/2008GL033194.

Stock, M., M. Akita1, P. Krehbiel, W. Rison, H. Edens, Z. Kawasaki, and M. A. Stanley (2014), Continuous broadband digital interferometry of lightning using a generalized cross-correlation algorithm, *J. Geophys. Res.*, *119*, 1–32, doi:10.1002/2013JD020217.

Wu, T., S. Yoshida, T. Ushio, Z. Kawasaki, Y. Takayanagi, and D. Wang (2014), Large bipolar lightning discharge events in winter thunderstorms in Japan, *J. Geophys. Res.*, *119*, 1–12, doi:10.1002/2013JD020369.